Defect-related multicolour emissions in ZnO tetrapods: from violet, over green to yellow

Miao Zhang, Frédéric Averseng, Francia Haque, Patrizia Borghetti, Jean-Marc Krafft, Benoît Baptiste, Guylène Costentin, Slavica Stankic

Defect-related multicolour emissions in ZnO tetrapods: from violet, over green to yellow

Miao Zhang[1,2] Frédéric Averseng[1], Francia Haque[2], Patrizia Borghetti[2], Jean-Marc Krafft[1], Benoît Baptiste[3], Guylène Costentin[1*] and Slavica Stankic[2*]

[1]Sorbonne Université, CNRS, Laboratoire de Réactivité de Surface, LRS, F-75005 Paris, France

[2]Sorbonne Université, CNRS, Institut des NanoSciences de Paris, INSP, F-75005 Paris, France.

[3]Sorbonne Université, CNRS, Institut de Minéralogie, de Physique des Matériaux et de Cosmochimie, IMPMC, F-75005 Paris, France

[*]Corresponding authors: guylene.costentin@upmc.fr and slavica.stankic@insp.jussieu.fr

ABSTRACT

The nature of defects in ZnO smoke was studied at different stages of the materials' history by combining photoluminescence (PL) and electron paramagnetic resonance (EPR) spectroscopies. In contrast to studies previously reported on ZnO nanopowders, high vacuum conditions ($P < 10^{-5}$ mbar) have been applied during sample's storage, handling and spectroscopic investigations. Two pairs of violet-PL/EPR signals (2.88 eV / g = 1.956 and 2.80 eV / g = 1.960) were observed in the as-synthesized ZnO powder and attributed to surface (dominant) and bulk zinc interstitials (Zn_i^+). Upon annealing in O_2-poor conditions, green-PL emission (2.41 eV) and EPR at g = 2.002 develop along with EPR signals specific of superoxide radicals (O_2^-). In absence of any external O_2 supply, the oxygen necessary for the creation of notable amount of O_2^- is provided by the lattice of ZnO smoke, so that the green emission, and its EPR counterpart, are unambiguously assigned to singly charged oxygen vacancies (V_o^+). Annealing in high P_{O2} results in a broad yellow-PL emission (~2.07 eV) without an EPR counterpart, and was assigned to peroxide-like surface species (O_2^{2-}). Overall, this study shows that the visible emissions in ZnO smoke nanopowders can range from violet, over green to yellow as a function of sample's

history and that the corresponding PL/EPR fingerprints can serve as guidelines for the recognition of defects in other ZnO types.

Keywords: ZnO, nanoparticles, defects, PL emission, EPR

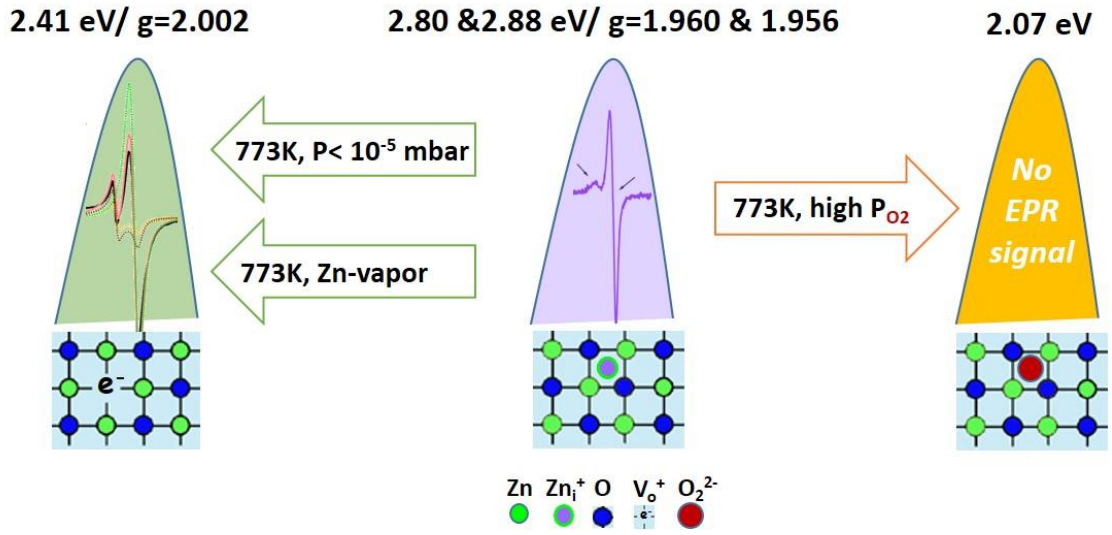

1. INTRODUCTION

The properties and, thus, technological potential of any semiconductor (chemical, optical, magnetic, etc.) are highly governed by the atomic-scale defects it contains. This applies to both the nature and quantity of defects that are present. A semiconducting metal oxide, ZnO, finds applications as a transparent conducting oxide for solar cells,[1, 2] piezoelectric for various electronic devices,[3] transparent thin film for gas sensors,[4, 5] nanowire-based gas sensor for NO_x or H_2,[6] UV optical emitter in LEDs,[7-9] and dilute magnetic semiconductor for spintronics.[10, 11] The presence of lattice defects is known to impact the performance of ZnO in most of these application fields. In particular, defects are highly undesiderable in ZnO used as UV optical emmiter in LEDs since their presence lead to lower luminescent efficiency when compared to a defect-free material. Hence, a fundamental knowledge on ZnO defects is required in order to tune the ZnO performances for a variety of novel high-tech applications.

Point defects are present in all crystalline materials in forms of missing (vacancies), interstitial (interstitials) or substituted (anti-sites) ions and are, generally, electronically charged. They induce local changes and lattice relaxations and new electronic states are generated within the band gap. The identification of crystal defects is, however, not a simple task. This can be illustrated by highly controversial assignments of photoluminescence (PL) and electron paramagnetic resonance (EPR) data reported for ZnO, with several defects proposed for a given signal or several signals ascribed to a given defect. This concerns in particular, the highly discussed green luminescence (centered ~2.17-2.5 eV) that was controversially assigned to a various ZnO defects (V_o, O_{Zn}, O_i, V_{Zn}).[12-19] The absence of consensus results from both, an inadequate comparison of samples of different origins (for instance single crystals vs. nanostructured ZnO) and/or the variability of experimental conditions applied during the synthesis, processing and measurements. The nature and concentration of a given defect depend strongly on all stages of the sample's history (from synthesis, over processing to measurements) and the corresponding spectroscopic properties are thus expected to vary. This particularly concerns nanostructured ZnO (nanoparticles, thin films) where, for instance, the measurements in air can strongly differ from those in vacuum.[20, 21] Another illustration is the transformation of an existing defect into a new one through the change of its oxidation state or the interaction with surrounding molecules, leading to the disappearance of its specific spectroscopic signal. For instance, oxygen vacancies can be efficiently passivated by water – as clearly demonstrated in FTIR studies on ZnO nanoparticles.[22-24] Therefore, exposing ZnO nanoparticles to a water-containing environment is likely to severely hinder the identification of native oxygen vacancies initially present in the sample.

Also, while theoretical calculations may provide useful information for the identification of lattice defects in ZnO, one should keep in mind that they are commonly performed at T = 0 K, i.e. far from the conditions usually achieved in experiments. Additionally, nanostructured

systems are usually obtained and studied far from thermodynamic equilibrium. Thus, the straightforward application of such theoretical results for discussing the existence of given defects is at least questionable. For example, because the formation energy of singly charged oxygen vacancies (V_o^+) was calculated to be rather high in ZnO,[25] the V_o^+ is therefore considered to be a defect rather difficult to create. Yet the present study will unambiguously prove otherwise.

In this contribution, by using highly controlled experimental conditions, we will demonstrate a close correlation of PL/EPR signatures to corresponding point defects observed on ZnO smoke nanopowder at different stages (as-synthesized, in the presence of O_2 and H_2O molecules, after thermal post-growth treatments). In that context, we applied the following strategy:

i) Use of clean synthesis route to exclude extrinsic defects thus limiting the investigation to the sole intrinsic ones.

ii) Application of high-vacuum conditions ($P < 10^{-5}$ mbar) during the storage, handling, and spectroscopic characterizations.

Such strategy allowed us to identify the nature of defects that are natively present in ZnO smoke and to follow their evolution as well as the appearance of new ones at different processing stages.

2. EXPERIMENTAL DETAILS

Synthesis and storage. ZnO smoke nanopowder was produced by metal combustion method in a glove box where the ignition of metallic Zn-foil of high purity (99.99%, 0.125 mm thickness, Advent Research Materials Ltd) was resistively induced.[26] As confirmed by XPS analysis, these synthesis conditions ensure that the formation of extrinsic defects was avoided. The white powder was collected on a glass plate and, then, transferred into a quartz-glass cell dedicated

to PL or EPR measurements. The powder was constantly maintained under dynamic vacuum ($P < 10^{-5}$ mbar) during the storage and *in situ* spectroscopic measurements.

Electron Microscopy. For the purpose of microscopic studies, as-synthesized ZnO powders were directly deposited on TEM grids, preventing the use of any solvent. Transmission electron microscopy (TEM) measurements were performed on a JEOL 2100 field emission transmission electron microscope operating at 200 kV with a 0.18 nm resolution. Scanning electron microscopy (SEM) images were recorded on a field emission Zeiss Supra 40 scanning electron microscope.

X-Ray Diffraction. X-Ray powder diffraction measurements were carried out at the X-ray diffraction platform of IMPMC on a Panalytical XpertPro MPD diffractometer using Co Kα radiation source ($\lambda_{K\alpha1}$ = 1.78897 Å, $\lambda_{K\alpha2}$ = 1.79285 Å) and an X'Celerator detector. The samples were prepared within a glove box and mounted in a homemade chamber allowing XRD measurements in controlled, anoxic conditions.

Cell parameters, mean coherent domain sizes and microstrain were refined using the Rietveld method as implemented in the Fullprof software. Since the peak width was larger than the instrumental resolution, lorentzian isotropic size (Y) and lorentzian isotropic strain (X) parameters were refined. The two effects can be decoupled on the diagram measured over a wide angular range because the first induces a peak broadening as Y/cos(theta) whereas the second as X/tan(theta).

Electron Paramagnetic Resonance (EPR).

In order to strictly control the different thermal treatments and subsequent EPR measurements, the following procedure has been followed: (i) a homemade setup equipped with a tubular oven has been used for all thermal treatments. High-vacuum was reached ($P < 10^{-5}$ mbar) using a turbo-molecular pump. Connections also permitted the controlled addition and removal of gases,

such as O_2 and H_2O vapor, during or after the thermal treatments. (ii) The ZnO sample was treated and measured in a suprasil quartz tube (5mm external diameter), combined with a high-vacuum bellow-type metal-glass stopper and ball joint, which allowed for a continuous connection with the homemade setup during all treatments, measurements, avoiding any unwanted external contamination.

The EPR measurements were performed on a JEOL FA300 computerized spectrometer working at ~9.3 GHz (X-band). All spectra were recorded placing the powders under dynamic vacuum ($P < 10^{-5}$ mbar) at 77 K, using an insertion dewar containing liquid nitrogen, applying a microwave power of 2 mW and 100 kHz field modulation and presented, as is usual, as the first derivative of the absorbance. In order to avoid the overmodulation and subsequent alteration of narrow EPR signals (resulting in signal broadening, loss of close peaks or multiplets, etc.), a modulation width/amplitude of 0.1mT was systematically used. The g-factors were calibrated by using solid 2,2-diphenyl-1-picrylhydrazyl (DPPH, g = 2.0037)) and care was taken to always keep the same height of powder in the EPR tube (~2 cm).

Additionally, g-factor of solids can be anisotropic (value differs among the considered direction), and is thus described as a tensor (3x3 matrix with zero non-diagonal terms, and g_x, g_y and g_z diagonal terms). Three cases may then occur: rhombic ($g_x \neq g_y \neq g_z$), axial ($g_z \neq g_x = g_y$), or isotropic ($g_z = g_x = g_y = g$) symmetry.[27] Computer simulations of the spectra were performed using the EPRsim32 program.[28]

Diffuse reflectance UV-vis (DR UV-Vis). The spectra were acquired at room temperature using a Varian Cary 5000 spectrometer equipped with an integrating sphere, while a sample of barium sulfate ($BaSO_4$) with ~100 % reflectance was used as a reference.

Photoluminescence (PL). Room-temperature experiments were performed on a Flurolog II fluorometer (Jobin-Yvon) equipped with a 450 W Xe lamp as an excitation source. Photoluminescence emission spectra were obtained fixing the excitation energy at 4.13 eV (300

nm) and using a WG-320 cut-off filter on the emission side to prevent the contributions of the first- and second order coming from excitation light. The PL band fitting analyses were done by using IGOR.

Photoluminescence and UV-vis diffuse reflectance measurements were carried out in a quartz glass tube that was connected to the same homemade high vacuum line ($P < 10^{-5}$ mbar) as that used for EPR measurements.

To investigate the impact of annealing steps in oxygen rich atmosphere (Section 3.2.2), the sample was alternatively annealed in P_{O2} = 100 mbar, then outgassed at room temperature to $P < 10^{-5}$ mbar for 1 h before the PL / EPR spectra were recorded under dynamic vacuum as usually. The same procedure was repeated in the second and third cycle.

Raman. The same quartz glass cell as described for PL and UV experiments was used for Raman investigations. Raman spectra were recorded at room temperature on a Jobin-Yvon triple-stage T64000 Raman spectrometer that is equipped with a CCD camera. An Argon laser monochromatic source (λ= 514.5 nm) was used.

X-ray photoelectron spectroscopy (XPS). XPS spectra were obtained with a non-monochromatic Al Kα source (photon energy, hν = 1486.7 eV) and a hemispherical analyzer Phoibos 100 with a pass energy of 20 eV at normal emission. The stoichiometric ratio n_1/n_2 between two species distributed homogeneously in the sample is obtained through the following equation: $n_1 / n_2 = I_1 \cdot (\sigma_2 \cdot \lambda_2 \cdot T_2) / I_2 \cdot (\sigma_1 \cdot \lambda_1 \cdot T_1)$, where I is the integration areas of the peak Zn 3s and that of the component of O 1s corresponding to lattice oxygen in ZnO, T is the transmission function of the analyzer tabulated for the analyzer Phoibos 100, λ_{Zn} and λ_O are provided by the NIST standard reference database for the ZnO material,[29, 30] while σ_{Zn} and σ_O are taken from references.[31]

3. RESULTS

3.1. As-prepared ZnO smoke nanoparticles

3.1.1. Morphological, Structural and Optical Properties

Figure 1a, b shows representative TEM images of as-prepared ZnO smoke nanoparticles. Rods (white arrow in Figure 1a) and tetrapods, with the latter being slightly dominant, were systematically observed in ZnO smoke micrographs. Such tetrapod-like structures, i.e. CdSe tetrapods, were shown to exhibit particular electron transport properties[32] and thus have recently gained a great attention. In these structures, four individual rod-like crystals (tetrapod-arms) grow from a common core and arrange together in the form of a tetrahedron. The length of the arms is larger than 100 nm while the diameter is clearly smaller than 50 nm. The high-resolution TEM (HRTEM) image of such a tetrapod arm seen along [021] zone axis is presented in Figure 1c. It illustrates that the tetrapod arms grow along the [0001] direction and have wurtzite structure. No disordered areas were observed and the lattice spacing was measured to be 0.281 nm, which matches with the d-spacing of {1011} ZnO planes. High crystal quality of particles is demonstrated by selected area electron diffraction (SAED) pattern (inset in Figure 1c).

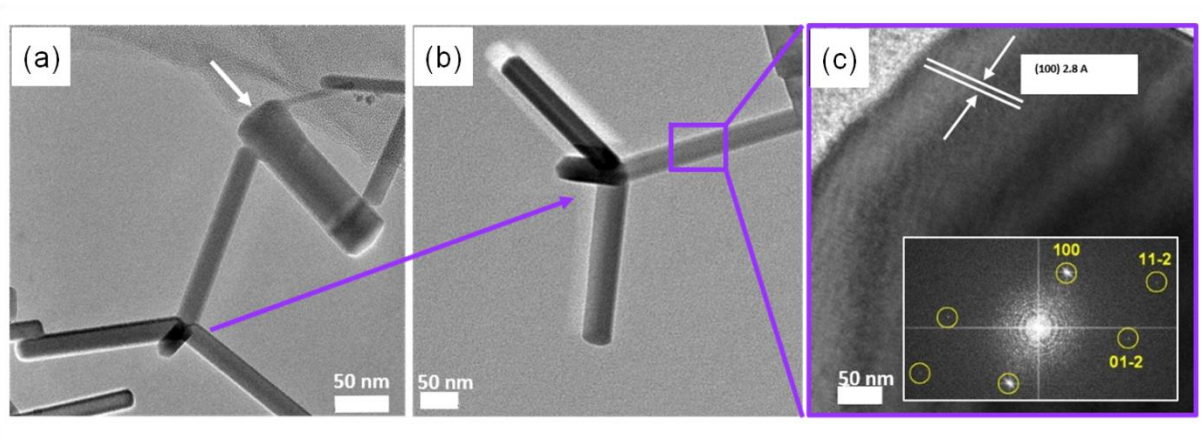

Figure 1. Representative TEM (a, b) and HRTEM (c) images of as-synthesized ZnO smoke sample. HRTEM image (c) corresponds to ZnO tetrapod arm viewed along a [021] zone axis of the wurtzite structure. The inset in (c) shows SAED of the selected HRTEM zone in violet.

The X-ray diffraction pattern (Figure 2a) and lattice parameters calculated by Rietveld refinement analysis (a = b = 3.250 Å, c = 5.207 Å, see Table I in Section 3.2.1) confirm the wurtzite phase. The intense and narrow diffraction peaks reflect the high crystal quality of the sample and a mean coherent domain size of ~ 90 nm. The microstrain, estimated by Williamson-Hall method[33] to be 3 %, indicates that the distances between the relevant crystal planes are not identical, pointing out some stress probably induced by the presence of defects. Raman spectrum (Figure 2b) reveals two intense peaks centered at 100 cm^{-1} (E_2^{low}) and 439 cm^{-1} (E_2^{high}). E_2^{low} and E_2^{high} Raman modes are particularly sensitive to the motion of zinc and oxygen in the lattice, respectively,[34, 35] and represent a direct measure of ZnO crystal quality. Additionally, two less intense peaks are observed at ~ 490 and at ~ 600 cm^{-1}. The former peak is usually detected on nanostructured ZnO and attributed to the surface optical phonon (SOP).[36] The broad and weak signal at 600 cm^{-1} can be correlated with the E_1(LO) peak previously detected on ZnO single crystals at ~ 590 cm^{-1} and assigned to intrinsic lattice defects.[35] In ZnO thin films grown in Zn-rich conditions, such a Raman mode at ~ 580-590 cm^{-1} was systematically attributed to an excess of zinc in the ZnO lattice, in line with the growth conditions.[37, 38]

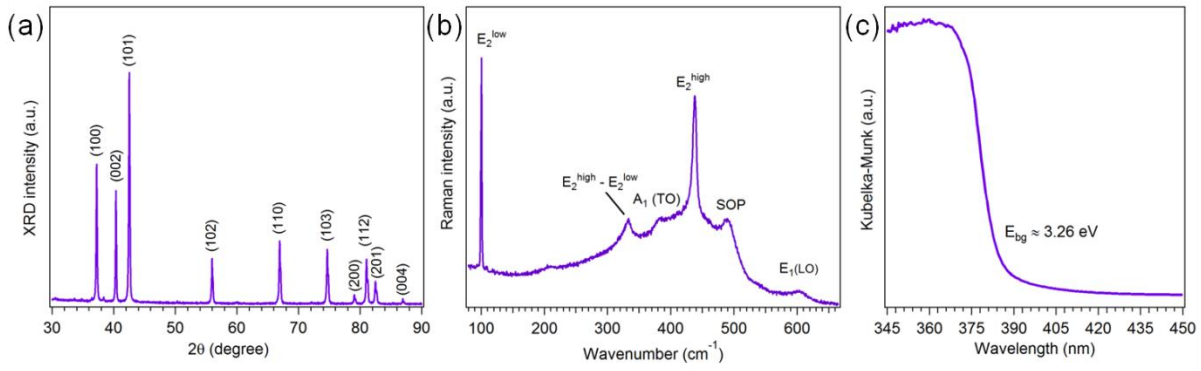

Figure 2. XRD pattern (a), Raman (b) and DR UV-Vis spectrum (c) of as-synthesized ZnO smoke.

The as-synthesized ZnO smoke powder exhibits white color and the related diffuse reflectance UV-visible spectrum (Figure 2c) shows an absorption threshold at ~ 380 nm. From the corresponding Tauc plot (Figure SI-1), the band gap energy (E_{BG}) was estimated to be 3.26 eV in line with values commonly reported for nanostructured ZnO (3.2 - 3.3 eV).[39, 40]

3.1.2. PL and EPR fingerprints of as-prepared ZnO smoke

Room temperature PL emission spectrum of the as-synthesized ZnO-smoke (Figure 3a) was obtained using an excitation energy of 4.13 eV that slightly exceeds the E_{BG} estimated from Tauc plot (Figure SI-1). The PL spectrum consists of a strong and sharp UV-band and a broad, low-intensity one in the visible domain. The UV-emission results from band-to-band transitions[13] and its high intensity reflects the good crystal quality demonstrated above by HRTEM, XRD and Raman data. The existence of an emission band in the visible domain, despite its low intensity, yet reflects that additional states exist in the band gap of the as-grown sample. Given the applied synthesis conditions, the native defects evidently present in ZnO smoke can only be of the intrinsic nature.

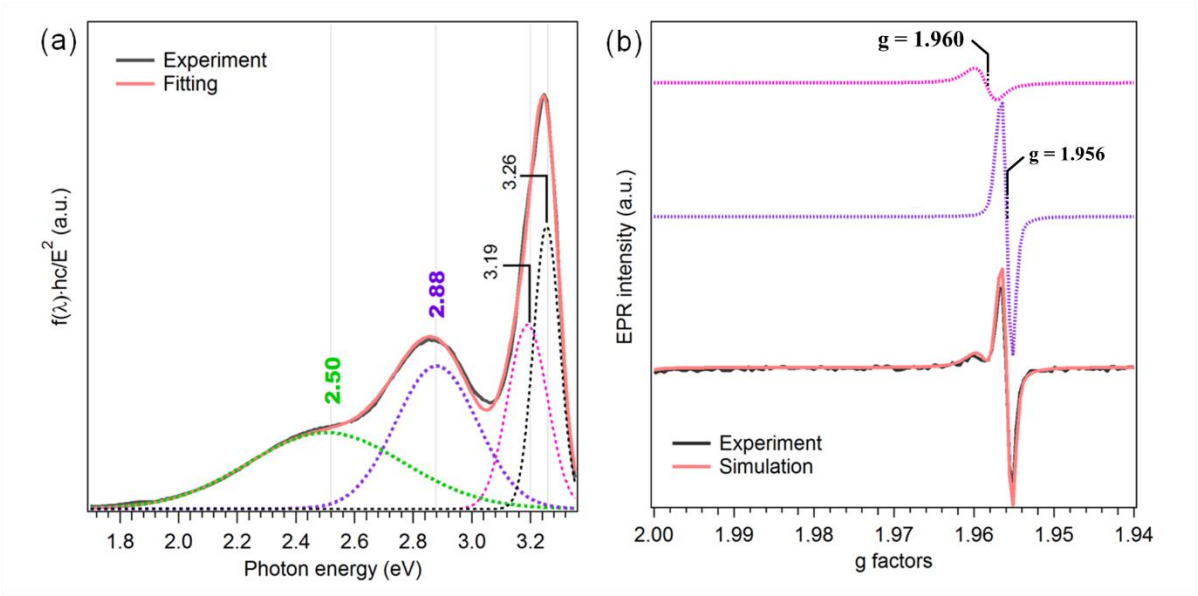

Figure 3. As-synthesized ZnO smoke: (a) PL spectra (black curve) and corresponding band-fitting analysis (red). The contribution of each emission is represented by dotted curves in black, magenta, violet and green. (b) Experimental (black curve) and simulated (red curve) EPR spectra. Violet and magenta dotted curves show the contribution of the two paramagnetic species (A and B).

Band fitting analysis (Figure 3a) shows that the PL spectrum can be nicely reproduced by a set of four Gaussian bands. The UV emission requires two Gaussians of similar energy (3.19 eV and 3.26 eV) – both close to the estimated value of E_{BG} (Figure SI-1). The width of the excitonic band and, so the necessity of two Gaussian curves for its adequate reproduction come from the morphological heterogeneity of the sample (Figure 1a). The visible emission can also be successfully fitted by a pair of Gaussians. The first one is centered at 2.50 eV (495 nm), which corresponds to green luminescence (GL) commonly reported in ZnO and, so far, attributed to all defects likely to be present in ZnO.[41-44] We will not discuss this PL band in the present paper since it is a subject of another ongoing study. The second Gaussian band reveals a slightly higher contribution and peaks at 2.88 eV (430 nm), an energy that matches with violet luminescence (VL). VL is less frequently measured on ZnO and observed on samples produced in non-equilibrium conditions followed by an ultra-rapid reactive quenching.[45] Unlike GL, for which no uniform recombination model was calculated, transitions between 2.75 and 2.90 eV have been quite consistently calculated to arise from energy states related to interstitial zinc (Zn_i).[46-48] The same assignment can also be found in several experimental studies.[38, 49, 50] VL observed in PL spectrum of as-synthesized ZnO smoke fits well to this interval suggesting Zn_i to be the defect specific of the applied synthesis method. This is not surprising since metal combustion synthesis occurs far from the equilibrium and includes rapid quenching conditions that, as mentioned above, favor Zn-rich ZnO. Such an excess of Zn, in at least the first few nanometers (~ 5 nm), of as–synthesized ZnO smoke surface was confirmed by XPS analysis (Zn/O = 1.26 ± 0.15).

EPR spectrum (Figure 3b) of the as-prepared sample consists of two signals: an intense and narrow signal at g = 1.956 (species A) and a weaker one at g = 1.960 (species B). EPR signals with g-value close to 1.960 have been often observed on ZnO yet without a consensus on their origin, so far.[51-57] Only a few studies report an EPR signal at g = 1.956 on ZnO,[58-60] yet Morazzoni and coworkers assigned it to Zn_i^+.[60] One should notice that this EPR signal prevails in the EPR spectrum of as-prepared ZnO smoke in the same way that VL was shown to dominate the visible domain of PL spectrum.

Considering the Zn-excess determined by XPS, the maximum of the visible PL and the synthesis conditions, we assign the two main PL/EPR features of as-grown ZnO smoke (Couple I: 2.88 eV / g = 1.956) to Zn_i^+. Additionally, the proximity in g-values of the two EPR signals (1.960 vs. 1.956) may point to the same type of species (i.e. Zn_i^+) yet experiencing a somewhat different crystallographic environment. In order to get more insights on that point, the impact of molecular oxygen on these two signals was further investigated since only defects located in the surface can be available for such interaction that would modify their corresponding signals.

3.1.3 Adsorption of O_2 at RT

Figure 4a compares the PL spectra of the as-synthesized ZnO (violet, solid line), in the presence of O_2 (orange, P_{O2} = 10 mbar) and after pumping out oxygen (violet, dotted line). Overall, the PL intensity decreases in the presence of O_2. It is well known that the adsorption of an e^- acceptor (such as O_2) on semiconductors surface leads to an upward band bending that, consequently, results in the generation of a depletion layer near the surface.[61, 62] Such a depletion layer determines the depth of the active PL and, so, the photoluminescence yield. This explains why the otherwise dominant light emission mechanism measured for the as-prepared ZnO smoke (UV-emission) is almost one order of magnitude weaker in the presence of O_2. In

the case of nanoparticles such effect is even more pronounced, since much of the material is close to the surface and, thus, more affected by band bending. Similar effects occurring upon O_2 admission were reported for ZnO nanowires by Reshchikov and coworkers[63] who measured a much higher intensity of excitonic emission in vacuum than in ambient air pressure. Such O_2 effect known to affect the intensity and shape of the PL spectra illustrates how important it is to record PL spectra under dynamic vacuum to prevent misleading interpretation due to O_2 interfering effects.

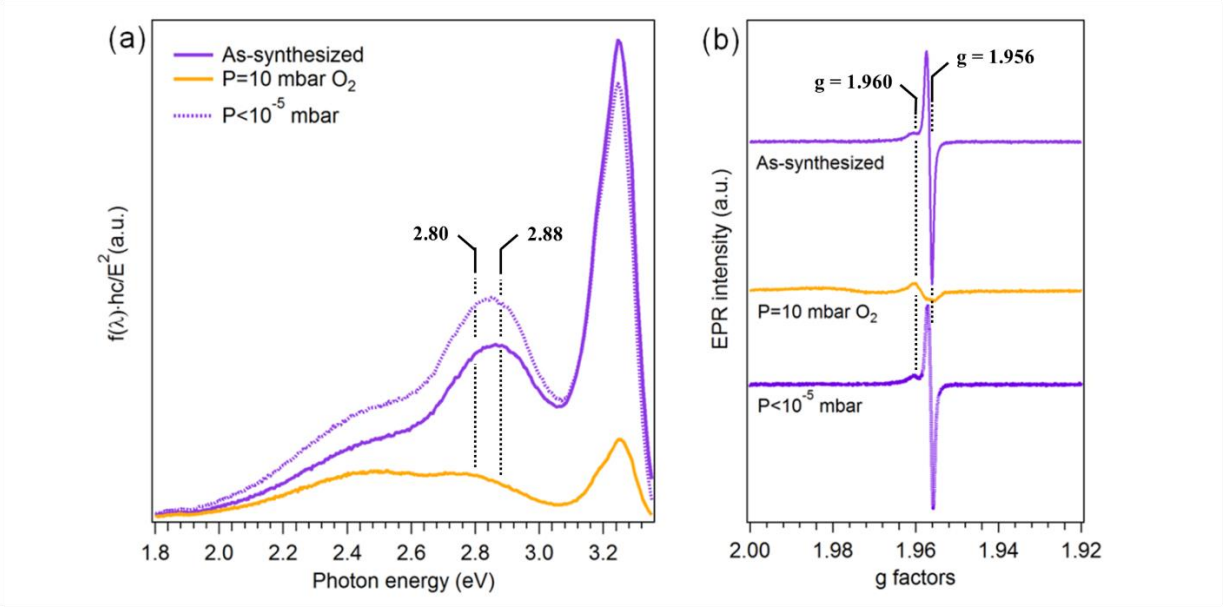

Figure 4. PL (a) and EPR (b) spectra of as-synthesized ZnO smoke in vacuum (solid violet curve), in presence of O_2 (solid orange curve, P_{O2} = 10 mbar) and after pumping out O_2 (dotted violet curve, P < 10^{-5} mbar).

On the other hand, a strong decrease of VL upon interaction with O_2 implies that the underlying defect (i.e. Zn_i^+) transforms into an optically inactive center. To be able to interact with gaseous O_2, Zn_i^+ defects must be located at the surface. Additionally, a PL band emerges at 2.80 eV (VL_B) upon O_2 adsorption. This band belongs also to the violet emission domain and was most probably already present in the spectrum of the as-synthesized sample yet, its contribution was

hardly distinguishable from the close and much more intense (four times) band at 2.88 eV. Hence, in a similar way to the coexisting EPR signals at rather close g-factors (g = 1.956 and 1.960), the two close violet bands (2.80 eV vs. 2.88 eV) are associated with defects of the same nature, yet localized in different environments – which is confirmed by their different reactivity towards oxygen.

In the EPR spectrum recorded under 10 mbar of O_2 (Figure 4b), the two close EPR signals (g = 1.956 and 1.960) also show opposite behaviors: while the one at g = 1.956 (species A) disappears almost completely (similarly to VL contribution in PL spectrum) the signal at g = 1.960 (species B) remains mainly unaffected (similarly to VL_B contribution in PL spectrum). After pumping O_2 out, the signal at g = 1.956 recovers back to its former state (dotted violet curve in Figure 4b), which points out a reversible process. Such a reversible broadening or, in our case, a complete disappearance (and recovery) of an EPR signal in the presence (and removal) of physically adsorbed O_2 – i.e. close enough to interact with the related paramagnetic species – is well reported in literature.[64, 65] Hence, the intensity decrease of the signal at g = 1.956 can be explained by strong dipolar interactions between adsorbed O_2 and paramagnetic Zn_i^+ from the surface.

Apart of being the dominant contributions in the initial spectra, VL at 2.88 eV and EPR signal at g = 1.956 show also a similar sensitivity towards O_2. These two contributions (Couple I) are therefore both assigned to surface Zn_i^+ and identified as the main native defects in ZnO smoke. We also note the recovery of Couple I signals to their initial state after pumping the O_2 out (dotted violet curves in Figure 4). This points towards rather weak O_2 adsorption and reversible electron transfer.

The pairing of the second couple (2.80 eV / g = 1.960; Couple II) is based on a similar reasoning: relatively lower contributions in initial PL/EPR spectra compared to those associated with

couple I, and similar tendencies upon O_2 addition. The couple II exhibits PL maxima and g-values only slightly different from those of couple I while not being affected by added O_2, and, therefore, can be attributed to the same type of defect, i.e. Zn_i^+, yet present deeper in the bulk. This is in agreement with a recent work by Erdem et al.,[66] in which an EPR signal at g = 1.96 was suggested to originate from core defects of ZnO.[67]

3.2 Effects of annealing treatments

In order to follow the outcome of the Zn_i^+ native defects and the eventual creation of new defects, the as-synthesized sample was annealed in either O_2-poor or O_2-rich conditions. The newly observed spectroscopic features and the associated species or defects assignments are gathered in Table 1. The related processing protocols were adopted in line with formation energies calculated for various point defects in ZnO over a wide range of O_2 partial pressures.[25, 68]

3.2.1 Annealing in low P_{O2}

Annealing in high vacuum. Compared to the as-synthesized ZnO smoke, no substantial morphological or structural changes could be observed on the sample annealed at T = 773 K in high vacuum ($P < 10^{-5}$ mbar) (Figure SI-2). Though the crystalline mean size domain noticeably decreases, the lattice parameters remain unchanged and the microstrain moderately increased from 3 to 6 % (Table 2), which may be due to the formation of new defects in ZnO crystal.

Table 1: List of the correlated PL and EPR signals (Couple) and of the EPR or PL signals (not associated with any PL or EPR feature) that have been detected depending on the history of the smoke sample (as-synthesized and / or upon subsequent post treatments) and their proposed assignment.

E_{emiss} (Ev)/ g value		**Conditions for detection**	**assignment**
Couple I	2.88 eV / g = 1.956	as-synthesized smoke and Zn annealed sample (in lower relative amount) *(sensitive to O_2 adsorption)*	Surface Zn_i^+
Couple II	2.80 eV / g = 1.960	as-synthesized smoke and Vacuum annealed and Zn vapor annealed samples *(insensitive to O_2 adsorption)*	Bulk Zn_i^+
Couple III	~ 2.41 eV / g ~ 2.002	Vacuum and Zn-vapor annealed samples (high intensity) and oxygen annealed sample (weak intensity) *(sensitive to water adsorption)*	Oxygen vacancy V_o^+
EPR	g_z = 2.047-2.043; g_y = 2.009; g_x = 2.003	Vacuum annealed sample *(disappearance upon long time pumping)*	Superoxide species (O_2^-) adsorbed on the ZnO surface
PL	2.0 eV	Oxygen annealed sample *(disappearance after long time pumping associated with simultaneous recovery of surface Zn_i^+ features*)	Peroxide-like species O_2^{2-} in interaction with the ZnO surface
PL	2.5 eV	as-synthesized smoke	to be discussed in a forthcoming paper

Table 2. Comparison of lattice parameters, microstrain and mean coherent domain size of as-synthesized and vacuum-annealed (773 K, P < 10^{-5} mbar) samples, obtained via Rietveld analysis.

	Lattice parameters (Å)	Microstrain (%)	Mean coherent domain size (nm)
As-synthesized	a = 3.25019 (5) b = 3.25019 (5) c = 5.20709 (10)	3	90
Vacuum-annealed	a = 3.25009 (8) b = 3.25009 (8) c = 5.20700 (14)	6	51

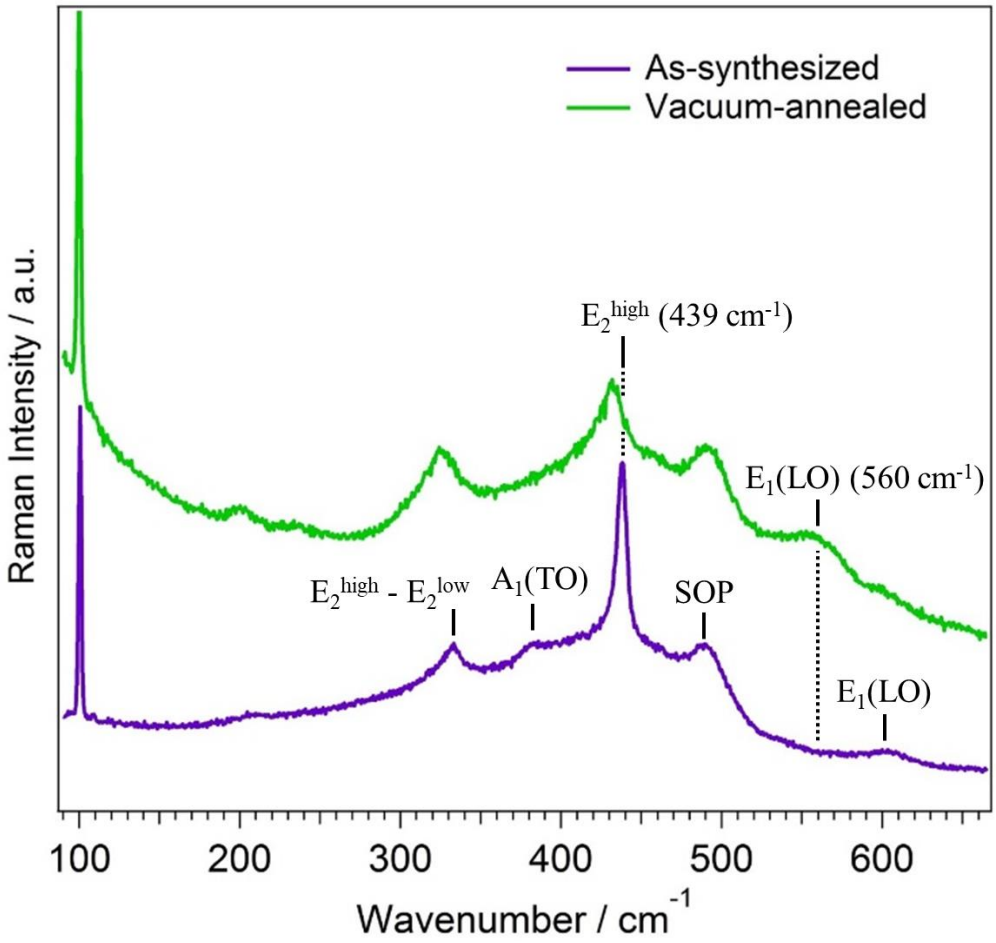

Figure 5. Raman spectra of as-synthesized and annealed (773 K, P < 10^{-5} mbar) ZnO smoke.

In the corresponding Raman spectrum (Figure 5, green curve), we observe that E_2^{high} peak (439 cm^{-1}), specific of lattice-oxygen motions, is strongly affected by such thermal treatment whereas a new E_1(LO) peak, specific of intrinsic defects, emerges at ~ 560 cm^{-1}.

The initially intense UV-emission (see Figure 3a) is strongly reduced upon annealing ZnO smoke to 773 K under high vacuum (P < 10^{-5} mbar) (Figure 6a) implying that a significant amount of defects is formed in the crystal where they provide new channels for electron-hole recombination. More interestingly, such annealing treatment results in a new PL band (Figure 6a) that can be reproduced by a single Gaussian curve centered at 2.41 eV (515 nm). Although mathematically not necessary for the resulting fit, one can notice that the VL ~2.80 eV may nevertheless be present in a small contribution within the new PL band. On the contrary, the VL ~2.88 eV remains rather undetectable.

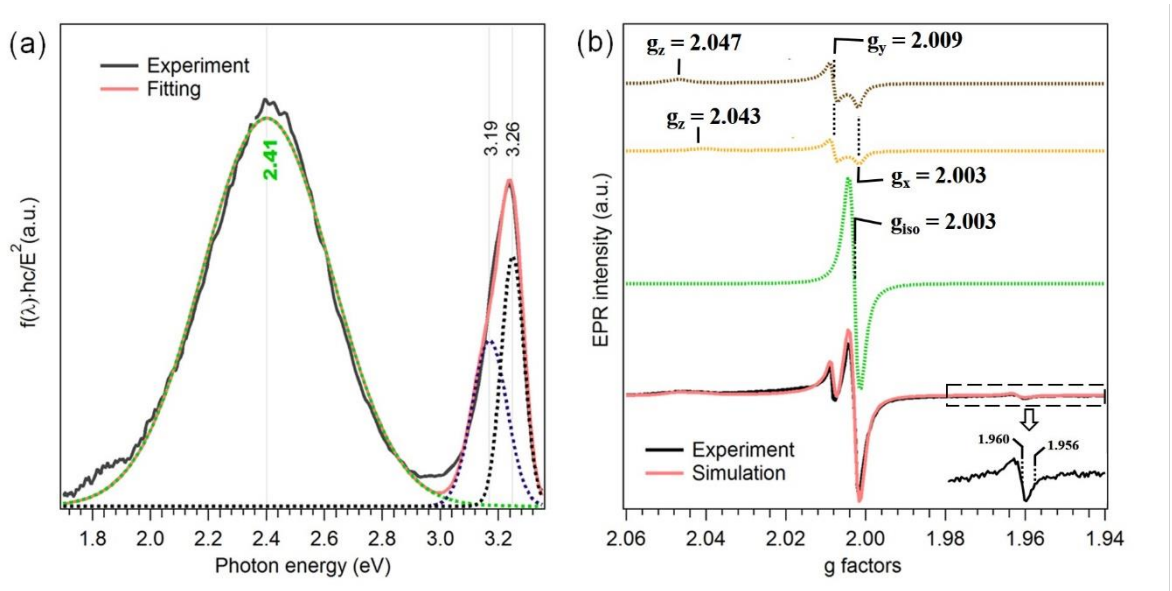

Figure 6. PL spectrum with corresponding band fitting (a) and experimental and simulated EPR spectra (b) of ZnO smoke annealed at 773 K in high vacuum (P < 10^{-5} mbar). Despite being shown in arbitrary units, the y-scales in Figure 6 are almost one order of magnitude lower than in Figure 3.

The corresponding EPR spectrum is shown in Figure 6b. When compared to that obtained on as-synthesized sample (zoom in Figure 6b vs Figure 3b), the signal at g = 1.956 is not detected anymore, whereas that at signal at g = 1.96 is comparatively not modified. The behavior of the former signal upon high-vacuum annealing is comparable to that of VL (2.88 eV), as it is also the case upon interaction with O_2. This strongly confirms the attribution of both spectroscopic features (couple I) to the same defect.

Simultaneously with the disappearance of the EPR signal at g = 1.956, a new signal is observed at g > 2.00. The EPR spectrum is rather complex in this range and the simulation (Figure 5b) shows contribution of three overlapping signals:

I. g_{iso} = 2.002 (species C, green doted)

II. g_z = 2.043, g_y=2.009 and g_x=2.003 (species D, yellow dotted)

III. g_z = 2.047, g_y=2.009 and g_x=2.003 (species E, brown dotted)

The origin of an isotropic EPR signal (species C) detected on ZnO with the g-value close to 2.00 remained a matter of great debate until present. Besides resonating close to the value of free electrons (g = 2.002) – attribution adopted by some authors[69, 70] – defects such as V_{Zn}:Zn_i complexes,[71] Zn_i^+,[72] Vo^{+}[69] and O_s^-[73] were also suggested. The other two signals detected in EPR spectrum of vacuum-annealed sample (species D and E) present a pseudo-axial rhombic symmetry consistent with superoxide species (O_2^-) adsorbed on ZnO.[60, 74-76] The g_z component is known to be the most sensitive to the environment of the paramagnetic species, so that its variation in species D and E may point out different localizations of O_2^- – yet both on the surface. The presence of superoxide anions on sample only annealed in high vacuum and measured upon continuous pumping ($P < 10^{-5}$ mbar) is, at first, surprising since the generation of such radicals generally occurs when a previously reduced surface is contacted with gaseous O_2.[75-77] It is

therefore evident that, here, for the creation of notable amount of O_2^- upon vacuum annealing, oxygen must have an intrinsic origin and, therefore, comes from the lattice of ZnO smoke. The evident loss of lattice oxygen can proceed via one of the following processes, each of them involving the concomitant formation of an oxygen vacancy (V_O^0, V_O^+ or V_O^{++}):

(1) $ZnO \xrightarrow{\Delta, vac} ZnO_{1-n} + nV_o^0 + n/2\ O_2$

(2) $ZnO \xrightarrow{\Delta, vac} ZnO_{1-n} + nV_o^+ + n/2\ O_2^- + n/2\ e^- \xrightarrow{\Delta, vac\ 20h} ZnO_{1-n} + nV_o^+ + n/2\ O_2 + ne^-$

(3) $ZnO \xrightarrow{\Delta, vac} ZnO_{1-n} + nV_o^{++} + n/2\ O_2^- + 3n/2\ e^- \xrightarrow{\Delta, vac\ 20h} ZnO_{1-n} + nV_o^{++} + n/2\ O_2 + 2ne^-$

Pathway (1) considers the formation of a neutral oxygen vacancy. There is no associated electron release required for the formation of O_2^-, although observed via corresponding EPR signals, nor any paramagnetic species that might stand for the EPR signal at g = 2.002 observed along with those of O_2^-. Pathway (3) implies the formation of a doubly charged oxygen vacancy V_O^{++}, fulfilling the conditions of e^- release and potentially explaining the formation of O_2^-. Yet, it still does not explain the signal at g = 2.002. Thus, only pathway (2) can completely explain the changes observed in EPR spectra upon high-vacuum annealing: departure of oxygen from the lattice and release of electrons associated with the formation of O_2^- and of paramagnetic V_o^+ species.

Considering the calculated formation energies of oxygen vacancies in ZnO[47, 78, 79] the absolute values greatly differ as a function of the calculation method. However, irrespectively of the calculation method used, the trend in E_f is rather constant in these studies: while the neutral oxygen vacancy was systematically reported to exhibit the highest E_f value, the formation of V_o^{++} was shown to be favorable in O-poor conditions.[25, 68, 78] The formation energy of a neutral oxygen vacancy V_O^0 was calculated in references [25] and [80] to be ~ 3.5 eV that should prohibit its presence even in an extremely O-poor condition. Nevertheless, when passing to

nanostructured systems the formation energy of the defect can be considerably lowered – as recently shown for V_o in ZrO_2[81] and on ZnO.[82] Still, one has to be careful not to rely too strictly on these results since calculations are performed at T = 0 K, generally far from most experimental conditions, and especially ours. For instance, although the V_o^+ is consistently reported as instable and observable only under irradiation[80], thus seemingly contradicting at first our experimental evidence, the O_2^- formation shown in our EPR spectrum strongly supports its presence in annealed ZnO smoke.

In conclusion, we cannot exclude any of the reaction pathways represented by (1-3), but only pathway (2) can explain the changes observed in EPR spectra upon high-vacuum annealing: (i) release of electrons necessary for the formation of O_2^- (specific EPR signals observed) and (ii) formation of an additional paramagnetic species which resonates at g = 2.002. Thus the EPR signal at g = 2.002 as well as its PL counterpart, measured on the same sample with maximum at 2.41 eV, can be quite assuredly assigned to V_o^+ (Couple III). We also note that the PL peak is rather broad and, although it can be represented by a lone Gaussian curve, it cannot be completely excluded that other contributions take also part – for instance, those that can be correlated to V_o and V_o^{++}, and which can be simultaneously formed following 1-3 pathways. This will be discussed in relation with the 2.5-2.2 eV PL emissions in a forthcoming paper.

Similar assignments for peaks of Couple III can be found in several studies.[83, 84] For instance, an emission band peaking at 2.43 eV was proposed as a result of the recombination between an e^- from an isolated V_o^+ vacancy and a photoexcited hole.[85] More recently, PL band at 2.45 eV was suggested to result from the $V_o^+ \rightarrow$ valence band transition.[86] However, since it was detected in extremely different and mostly uncontrolled experimental conditions, no consensus is yet reached for its assignment. In addition, different transitions matching this energy were calculated by several groups.[87-89] Finally, this led to the fact that several defects likely to exist

in ZnO were suggested as candidates for this PL band. The attribution of the EPR signal at g=2.002 is, on the other hand, hindered by the fact that it lies very close to the value usually reported for free electrons (g ~ 2.00). However, the *in situ* (dynamic vacuum, $P < 10^{-5}$ mbar) detection of O_2^- specific EPR signals in our experiment confirms that oxygen is released from the Zn-O network and O-vacancies must have subsequently been formed – and related to the signals of Couple III.

We have furthermore noticed that the O_2^- specific EPR signals, detected in the course of high-vacuum annealing, disappear when the sample is subjected to a longer pumping time at room temperature (t > 20 h). Evidently, O_2^- species can be fully removed in the form of O_2 through a fully reversible electron transfer at room temperature – a typical behavior of superoxide species. In contrast, the 2.41 eV and g = 2.002 couple (couple III) were still detected after 20h pumping at RT, indicating that V_o^+ vacancy is stable upon time.

The loss of lattice oxygen occuring upon annealing under vacuum explains also the intensity decrease of the signals related to surface Zn_i^+ (couple I). Indeed, apart from the fraction of released electron necessary for O_2^- formation, pathway (2) also provides electrons that may interact with surface Zn_i^+ and transform them into Zn^0. Part of this Zn^0 is most probably sublimated at these temperatures and, thus, removed from the system. Indeed, once the annealing treatment was completed a greyish deposit was observed on the cold part of either the PL or EPR cells. This is supported by XPS indicating a decrease of the Zn/O ratio of the annealed sample (1.10) compared to that obtained on as-synthesized ZnO smoke (1.26). Figure 7 reports a synoptic proposal for the interconnected redox processes occurring upon vacuum annealing treatment and that are responsible for the disappearance of some native defects and generation of new ones.

Figure 7: Diagrammatical representation of the defects detected along the history of the smoke ZnO sample, starting from as-synthesized to post annealing treatments either in low P_{O2} (vacuum and Zn-vapor atmospheres) or in high P_{O2} atmospheres, in relation with the qualitatively interconnected redox processes occurring, depending on the operating conditions. Native defects in ZnO smoke, i.e. bulk and surface Zn_i^+ are reduced upon annealing in low PO_2 by electrons released by the formation of oxygen vacancies. During the annealing in high PO_2, antagonistic processes occur leading, on the one hand, to the oxidation of Zn_i^+ defects and formation of peroxide-like species, and, on the other hand, to oxygen vacancy formation.

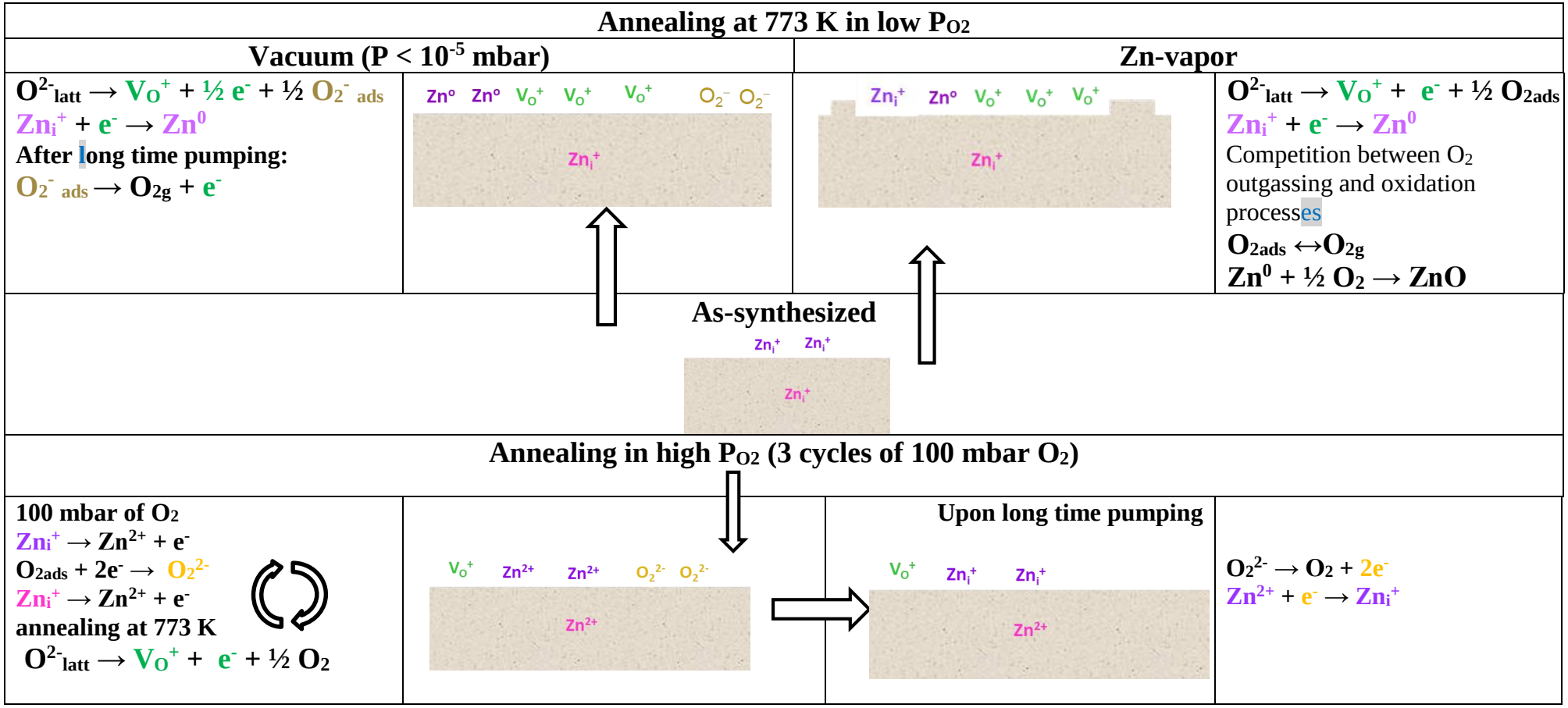

The assignement of couple III to V_o^+ is also supported by investigating the expected reactivity of water on such defect[23, 88], as shown in figure 8. Water splitting fills up the V_o^+ vacancy, leading to the intensity decrease of couple III. Moreover, the associated released electron interacts with surface Zn^{2+} and forms Zn^+, explaining the concomitant intensity increase of the couple I (VL at 2.88 eV and g= 1.956), as described in equation (4):

(4) $V_o^+ - Zn^{2+} - O^{2-} + H_2O \rightarrow [H-O]^- - Zn^{2+} - [H-O]^- + \bullet \rightarrow [H-O]^- - Zn^+ - [H-O]^-$

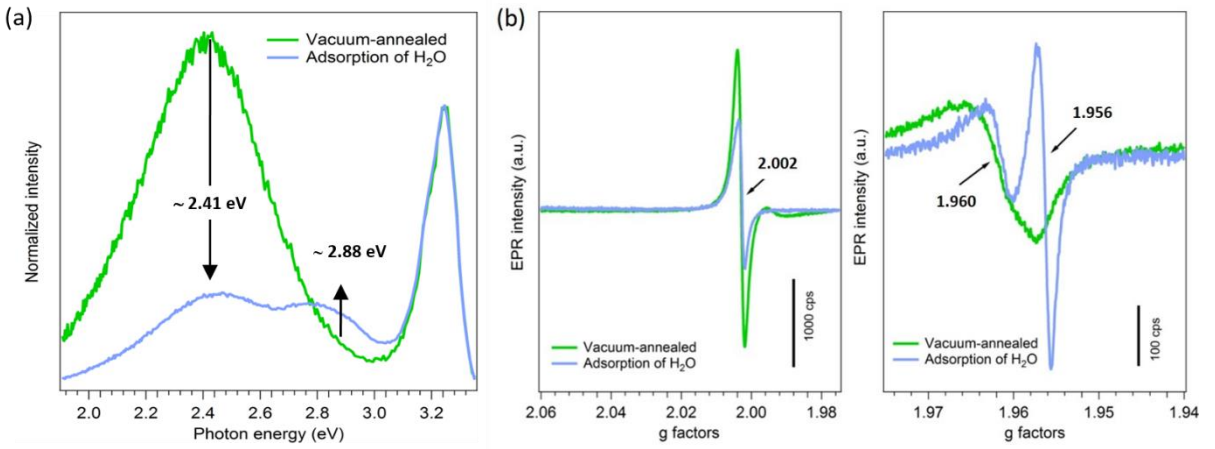

Figure 8 :(a) PL spectra and (b) EPR spectra of high vacuum annealed ZnO smoke (773 K and $P < 10^{-5}$ mbar) and after exposing this powder to water (P_{H2O} = 10 mbar).

Annealing in Zn-vapor. PL and EPR spectra of ZnO smoke annealed in Zn-rich atmosphere are shown in Figure 9a and b, respectively. Both PL and EPR spectra show signals (at 2.41 eV (515 nm) and g = 2.002 (species C)) identical to those of the couple III observed on vacuum annealed ZnO smoke. This is not surprising since the formation of oxygen vacancies is expected under such experimental conditions applied – i.e. Zn-rich atmosphere. As in the case of the

vacuum annealed sample, the electron release upon formation of V_o^+ may once more explain the intensity decrease of spectroscopic fingerprints related to surface Zn_i^+ (couple I). The main difference compared to annealing in vacuum is that upon Zn-vapor annealing, D and E EPR species attributed to O_2^- species are not detected (Figure 6b, Table I). Such absence of the O_2^- specific signals is yet not surprising since Zn being present in excess in the gas phase so that the newly formed O_2 may rapidly react with gaseous Zn to form new ZnO entities (figure 7).

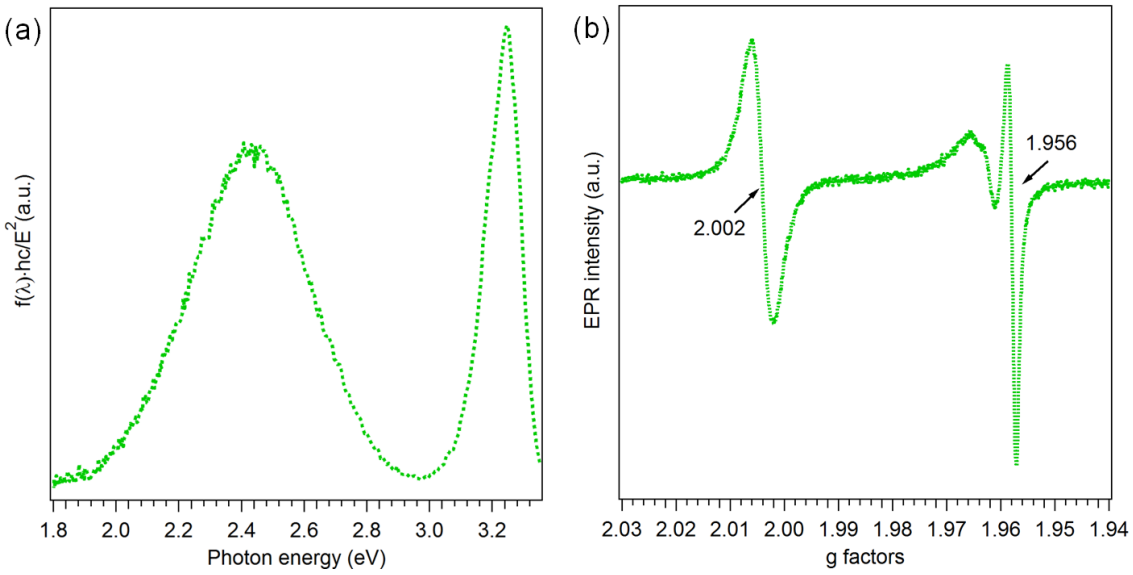

Figure 9. PL (a) and EPR (b) spectra obtained on ZnO smoke annealed at 773 K in the presence of Zn-vapor (P_{Zn} ~ 100 mbar).

3.2.2 Annealing in high P_{O2}

In another set of experiments, the sample was repeatedly annealed in oxygen and then outgassed. The PL spectra obtained after each of the 3 cycles are presented in Figure 10a. After the first cycle (brown curve), the intensity of VL (2.88 eV, surface Zn_i^+) decreased along with an intensity increase in the lower energy part (< 2.5 eV) of the spectrum. Both evolutions are further pronounced with every additional O_2 annealing/outgassing cycle. After the third cycle,

VL is completely absent, which can be explained by the oxidation of Zn_i^+ that is thus transformed into optically inactive Zn^{2+} centers. The intense PL band that develops at ~2.0 eV i.e. in the yellow part of the optical spectrum (600 nm, yellow luminescence (YL)) is rather broad and can be decomposed into more than one PL emission (Figure SI-3). Besides YL contribution at 2.07 eV, the one at 2.41 eV is also present, which is also confirmed by EPR signal at g = 2.002 (not shown) (Table 1). Interestingly, YL disappears after longer pumping time (24 h instead of usual 1h) (Figure 10b), suggesting that the underlying defect is weakly bound to ZnO.

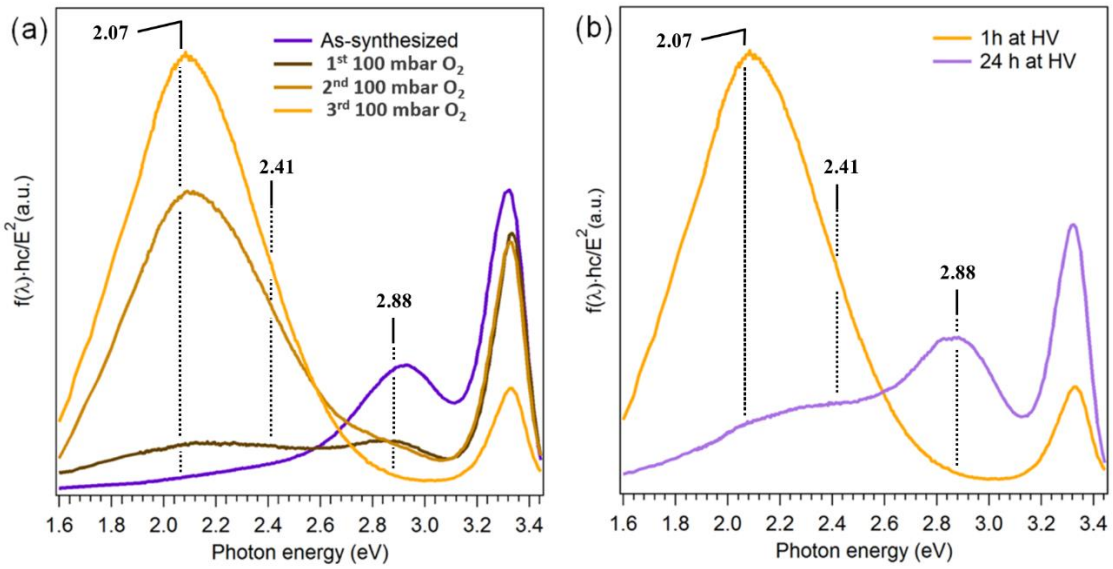

Figure 10. PL spectra (a) of ZnO smoke repeatedly annealed in O_2 (T_{ann} = 773 K, P_{O2} = 100 mbar) then outgassed at RT. (b) Comparison of PL spectra of the ZnO after three cycles recorded after 1h (yellow) and 24h pumping (light violet).

Whereas the evolution of yellow luminescence (YL) is not surprising – since it was systematically measured in oxygen rich conditions and on all forms of ZnO (single crystals,[90] thin films[91] and nanoparticles[20, 92, 93]) the coexistence of the PL / EPR fingerprints attributed to V_o^+ remains unusual at first glance (Table 1). However, considering the applied experimental

conditions the competition between three processes should be assumed: i) formation of V_o (due to high annealing T), ii) passivation of V_o (due to the presence of O_2) and iii) formation of defects related to YL emission (due to high P_{O2}) (Figure 7). Indeed, though O_2 is present during annealing, a competition between the generation and passivation of oxygen vacancies occurs, as demonstrated by Drouilly et al.[94]

Despite the rather high formation energies calculated for O_i-type defects, DFT stability diagrams show[25, 78] that these defects can be significantly favored in O_2 rich atmosphere. Therefore, the yellow luminescence was principally assigned to oxygen interstitials – more precisely to singly charged ones (O_i^-).[95-97] Based on the absence of a new EPR signal in the sample exhibiting YL, we have to exclude a paramagnetic nature of this defect. According to theory,[25, 98] O_i may not only be isolated, yet located close to lattice oxygen ions, giving rise to a molecular-like diatomic entity. Such entity would exhibit fully occupied ppπ* orbitals[25, 98], with an electronic structure similar to that of O_2^{2-} peroxide species. Therefore, in contrast to the generally accepted picture of singly charged oxygen interstitials (O_i^-) being assigned to yellow emission,[95, 97] we instead propose a peroxide-like entity stabilized at the surface of ZnO nanoparticles where it acts as the recombination center for YL. A similar scenario is demonstrated also in the case of NiO surface in Ref.[99]. Once at the surface, the oxygen molecule can be reduced to surface bidentate O_2^{2-} by electrons provided either via oxidation of Zn_i^+ or from oxygen vacancies – the formation of which was shown to be one of the competing processes in this experiment. Not dissociated, such peroxide-species can easily leave the surface as was confirmed by the disappearance of YL upon more efficient pumping (light violet curve in Figure 10b). In the same spectrum, the reversibility of such a process can be observed through the recovery of the Zn_i^+ characteristic signal. The attribution of YL to such O_2^{2-}bidentate, localized at the surface instead of being embedded in ZnO crystal – as suggested by Janotti et

al.[25] – may be questioned except if one considers the nano-nature of ZnO (Table 1, figure 7). At the same time, it opens up basis for new computational strategies.

4. CONCLUSIONS

By combining electron paramagnetic resonance (EPR) and photoluminescence (PL) spectroscopies, we have studied the nature of native defects in ZnO nanopowders prepared via metal combustion technique. Several processing protocols have been applied to follow the outcome of the existing defects and the eventual creation of new ones. Thanks to the strict control of the experimental conditions during all stages of sample's storage, processing and measurements, crystal defects are identified in correlation with the conditions-specific PL/EPR fingerprints.

We demonstrate here how important it is to precisely detail the experimental conditions in which spectra were recorded. Combining EPR and PL in controlled conditions allows the spectroscopic fingerprints to be unambiguously attributed to the corresponding defects. An example is the couple I (2.88 eV / g = 1.956) that otherwise escapes detection on nanostructured ZnO as due to O_2 or H_2O containing atmosphere applied during the measurements. The same is true for the identification of V_o^+ that could be missed if the corresponding measurements were not performed in conditions that ensure the detection of O_2^- specific signals i.e. in dynamic high vacuum ($P< 10^{-5}$ mbar). Moreover, thanks to the detection of O_2^-, the doubtless assignment of EPR at g = 2.002 to V_o^+ species provided a basis to exclude these defects to be present in as-synthesized sample and to attribute the observed couple I exclusively to Zn_i^+ – as additionally supported also by XPS results. We also showed that the use of probe molecules, such as O_2, may provide efficient discrimination between same defects yet localized in different crystallographic environment, namely surface or bulk.

Bulk and surface Zn_i^+ were identified as native defects specific of the applied synthesis method. Upon annealing in O_2-poor conditions, we undoubtedly demonstrate the formation of singly charged oxygen vacancies (V_o^+) on ZnO surface. Annealing in high P_{O2} was shown to lead to antagonism effects relative to high temperature and atmosphere, respectively. Apart from relatively small contribution of V_o^+ as due to high-annealing temperature applied, defects specific of O_2-rich conditions are produced in the form of peroxide-like diatomic oxygen. The various defects identified in this study were shown to produce color specific PL emissions that range from violet (Zn_i^+), over green (V_o^+) to yellow (O_2^{2-}) visible domain. Hence, under strictly controlled conditions, ZnO smoke can represent an appropriate model system for studying crystal defects. A great deal of cross-agreements between strictly controlled experimental conditions and PL/EPR fingerprints provides a simple approach that can be used for studying and/ or identifying defects in other ZnO types.

ACKNWOWLEDGMENT

Dr. Miao Zhang wants to thank the China Scholarship Council (CSC) for the three years Ph.D. founding. The authors are also grateful to: Vincent Losinho from Laboratoire de Réactivité de Surface, Sorbonne Université, (LRS) for his help in designing and building the set up used for EPR and PL *in situ* studies and Stephane Chenot from Institut des NanoSciences de Paris, Sorbonne Université, (INSP) for the maintenance of synthesis chamber and high-vacuum storage lines.

REFERENCES

1. S. Jung, J. Lee, J. Seo, U. Kim, Y. Choi and H. Park, *Nano Lett.*, 2018, **18**, 1337-1343.
2. H. Li, L. K. Schirra, J. Shim, H. Cheun, B. Kippelen, O. L. Monti and J.-L. Bredas, *Chem. Mater.*, 2012, **24**, 3044-3055.
3. S. Vishniakou, R. Chen, Y. G. Ro, C. J. Brennan, C. Levy, E. T. Yu and S. A. Dayeh, *Adv. Mater. Technol.*, 2018, **3**, 1700279.
4. M. S. Yao, W. X. Tang, G. E. Wang, B. Nath and G. Xu, *Adv. Mater.*, 2016, **28**, 5229-5234.
5. J.-W. Kim, Y. Porte, K. Y. Ko, H. Kim and J.-M. Myoung, *ACS Appl. Mater. & Interfaces*, 2017, **9**, 32876-32886.
6. A. Katoch, J.-H. Kim, Y. J. Kwon, H. W. Kim and S. S. Kim, *ACS Appl. Mater. & Interfaces*, 2015, **7**, 11351-11358.
7. W. Zhao, X. Xiong, Y. Han, L. Wen, Z. Zou, S. Luo, H. Li, J. Su, T. Zhai and Y. Gao, *Ad. Optical Mater.*, 2017, **5**, 1700146.
8. R. Bao, C. Wang, Z. Peng, C. Ma, L. Dong and C. Pan, *ACS Photonics*, 2017, **4**, 1344-1349.
9. M. D. Marcantonio, S. Gellner, J. E. Namanga, J. Frohleiks, N. Gerlitzki, F. Vollkommer, G. Bacher and E. Nannen, *Adv. Mater. Technol.*, 2017, **2**, 1600215.
10. A. Behan, A. Mokhtari, H. Blythe, D. Score, X. Xu, J. Neal, A. Fox and G. Gehring, *Phys. Rev. Lett.*, 2008, **100**, 047206.
11. Z. Sun, X. Yang, C. Wang, T. Yao, L. Cai, W. Yan, Y. Jiang, F. Hu, J. He and Z. Pan, *ACS Nano*, 2014, **8**, 10589-10596.
12. H.-L. Guo, Q. Zhu, X.-L. Wu, Y.-F. Jiang, X. Xie and A.-W. Xu, *Nanoscale*, 2015, **7**, 7216-7223.
13. P. Camarda, F. Messina, L. Vaccaro, S. Agnello, G. Buscarino, R. Schneider, R. Popescu, D. Gerthsen, R. Lorenzi and F. M. Gelardi, *Phys. Chem. Chem. Phys.*, 2016, **18**, 16237-16244.
14. R. Gurwitz, R. Cohen and I. Shalish, *J. Appl. Phys.*, 2014, **115**, 033701.
15. T. M. Borseth, B. G. Svensson, A. Y. Kuznetsov, P. Klason, Q. X. Zhao and M. Willander, *Appl. Phys. Lett.*, 2006, **89**, 262112-262111-262112-262113.
16. K. H. Tam, C. K. Cheung, Y. H. Leung, A. B. Djurisic, C. C. Ling, C. D. Beling, S. Fung, W. M. Kwok, W. K. Chan, D. L. Philips, L. Ding and W. K. Ge, *J. Phys. Chem. B*, 2006, **110**, 20865-20871.
17. B. Lin, Z. Fu and Y. Jia, *Appl. Phys. Lett.*, 2001, **79**, 943.
18. Z. Wang, X. Zu, S. Zhu and J. Wang, *Physica E*, 2006, **35**, 199.
19. J. Lv and C. Li, *Appl. Phys. Lett.*, 2013, **103**, 232114.
20. A. R. Gheisi, C. Neygandhi, A. K. Sternig, E. Carrasco, H. Marbach, D. Thomele and O. Diwald, *Phys. Chem. Chem. Phys.*, 2014, **16**, 23922-23929.
21. B. Fabbri, A. Gaiardo, A. Giberti, V. Guidi, C. Malagù, A. Martucci and M. Sturaro, *Procedia Engineering*, 2014, **87**, 148-151.
22. C. Drouilly, J.-M. Krafft, F. Averseng, H. Lauron-Pernot, D. Bazer-Bachi, C. Chizallet, V. Lecocq and G. Costentin, *Catal. Today*, 2013, **205**, 67-75.
23. H. Noei, H. Qiu, Y. Wang, E. Löffler, C. Wöll and M. Muhler, *Phys. Chem. Chem. Phys.*, 2008, **10**, 7092-7097.
24. F. Haque, S. Chenot, F. Viñes, F. Illas, S. Stankic and J. Jupille, *Phys. Chem. Chem. Phys.*, 2017, **19**, 10622-10628.
25. A. Janotti and C. G. Van de Walle, *Phys. Rev. B*, 2007, **76**, 165202.
26. S. Stankic, M. Cottura, D. Demaille, C. Noguera and J. Jupille, *J. Cryst. Growth*, 2011, **329**, 52-56.
27. J. A. Weil and J. R. Bolton, *Electron Paramagnetic Resonance- Elemental Theory and Practical Applications*, 2nd Edition, John Wiley & Sons, Inc., Hoboken, New Jersey, 2007.
28. T. Spalek, P. Pietrzyk and Z. Sojka, *J. Chem. Inf. Model.*, 2005, **45**, 18-29.
29. C. J. Powell and A. Jablonski, *NIST Electron Effective-Attenuation-Length Database - Version 1.3, National Institute of Standards and Technology.*, Gaithersburg, MD 2011.
30. X. Llovet, F. Salvat, D. Bote, F. Salvat-Pujol, A. Jablonski and C. J. Powell, *NIST Database of Cross Sections for Inner-Shell Ionization by Electron or Positron Impact, Version 1.0, National Institute of Standards and Technology*, Gaithersburg, Maryland, 2014.
31. J. J. Yeh, *Atomic calculation of photoionization cross-sections and asymmetry parameters*, 1985.
32. M. Karakus, Y. Sung, H. I. Wang, Z. Mics, K. Char, M. Bonn and E. Cánovas, *J. Phys. Chem. C*, 2017, **121**, 13070-13077.
33. P. Bindu and S. Thomas, *J. Theor. Appl. Phys.*, 2014, **8**, 123-134.
34. S. Kumar and P. Sahare, *Nano*, 2012, **7**, 1250022.
35. R. Cuscó, E. Alarcón-Lladó, J. Ibanez, L. Artús, J. Jimenez, B. Wang and M. J. Callahan, *Phys. Rev. B*, 2007, **75**, 165202.
36. H. Zeng, W. Cai, B. Cao, J. Hu, Y. Li and P. Liu, *Appl. Phys. Lett.*, 2006, **88**, 181905.

37. G. J. Exarhos and S. K. Sharma, *Thin Solid Films*, 1995, **270**, 27-32.
38. D. Thapa, J. Huso, J. L. Morrison, C. D. Corolewski, M. D. McCluskey and L. Bergman, *Opt. Mater.*, 2016, **58**, 382-389.
39. M. Miyake, M. Suginohara, N. Narahara, T. Hirato and P. V. Braun, *Chem. Mater.*, 2017, **29**, 9734-9741.
40. G. Ou, D. Li, W. Pan, Q. Zhang, B. Xu, L. Gu, C. Nan and H. Wu, *Adv. Mater.*, 2015, **27**, 2589-2594.
41. F. Leiter, H. Alves, A. Hofstaetter, D. Hofmann and B. Meyer, *Phys. Status Solidi (b)*, 2001, **226**, R4-R5.
42. A. B. Djurišić, W. C. Choy, V. A. L. Roy, Y. H. Leung, C. Y. Kwong, K. W. Cheah, T. Gundu Rao, W. K. Chan, H. Fei Lui and C. Surya, *Adv. Funct. Mater.*, 2004, **14**, 856-864.
43. M. Li, G. Xing, G. Xing, B. Wu, T. Wu, X. Zhang and T. C. Sum, *Phys. Rev. B*, 2013, **87**, 115309.
44. K. E. Knutsen, A. Galeckas, A. Zubiaga, F. Tuomisto, G. C. Farlow, B. G. Svensson and A. Y. Kuznetsov, *Phys. Rev. B*, 2012, **86**, 121203.
45. S. Polarz, A. Roy, M. Merz, S. Halm, D. Schröder, L. Schneider, G. Bacher, F. E. Kruis and M. Driess, *Small*, 2005, **1**, 540-552.
46. P. Erhart, K. Albe and A. Klein, *Phys. Rev. B*, 2006, **73**, 205203.
47. S. Zhang, S.-H. Wei and A. Zunger, *Phys. Rev. B*, 2001, **63**, 075205.
48. D. C. Look, G. C. Farlow, P. Reunchan, S. Limpijumnong, S. Zhang and K. Nordlund, *Phys. Rev. Lett.*, 2005, **95**, 225502.
49. H. Zeng, G. Duan, Y. Li, S. Yang, X. Xu and W. Cai, *Adv. Funct. Mater.*, 2010, **20**, 561-572.
50. M. Chen, Z. Wang, D. Han, F. Gu and G. Guo, *J. Phys. Chem. C*, 2011, **115**, 12763-12773.
51. K. Vanheusden, W. Warren, C. Seager, D. Tallant, J. Voigt and B. Gnade, *J. Appl. Phys.*, 1996, **79**, 7983-7990.
52. W. K. Liu, K. M. Whitaker, A. L. Smith, K. R. Kittilstved, B. H. Robinson and D. R. Gamelin, *Phys. Rev. Lett.*, 2007, **98**, 186804.
53. V. Ischenko, S. Polarz, D. Grote, V. Stavarache, K. Fink and M. Driess, *Adv. Funct. Mater.*, 2005, **15**, 1945-1954.
54. J. Qu, Y. Ge, B. Zu, Y. Li and X. Dou, *Small*, 2016, **12**, 1369-1377.
55. C. G. Van de Walle, *Phys. Rev. Lett.*, 2000, **85**, 1012.
56. S. Cox, E. Davis, S. Cottrell, P. King, J. Lord, J. Gil, H. Alberto, R. Vilao, J. P. Duarte and N. A. de Campos, *Phys. Rev. Lett.*, 2001, **86**, 2601.
57. A. W. Cohn, N. Janßen, J. M. Mayer and D. R. Gamelin, *J. Phys. Chem. C*, 2012, **116**, 20633-20642.
58. D. Hofmann, H. Zhou, D. Pfisterer, H. Alves, B. Meyer, P. Baranov, N. Romanov, C. de Mello Donega, A. Meijering and S. Orinskii, *Phys. Status Solidi (c)*, 2004, **1**, 908-911.
59. L. Larina, N. Tsvetkov, J. Yang, K.-S. Lim and O. Shevaleevskiy, *ECS Transactions*, 2010, **28**, 161-167.
60. F. Morazzoni, R. Scotti and S. Volontè, *J. Chem. Soc., Faraday Trans.*, 1990, **86**, 1587-1591.
61. Z. Zhang and J. T. Yates Jr, *Chem. Rev.*, 2012, **112**, 5520-5551.
62. S. Ma, M. E. Reish, Z. Zhang, I. Harrison and J. T. Yates Jr, *J. Phys. Chem. C*, 2017, **121**, 1263-1271.
63. M. A. Reshchikov, A. Behrends, A. Bakin and A. Waag, *J. Vac. Sci. & Technol. B*, 2009, **27**, 1688-1692.
64. R. Iyengar, V. S. Rao and A. Zettlemoyer, *Surf. Sci.*, 1969, **13**, 251-262.
65. V. J. Joly, K. Takahara, K. Takai, K. Sugihara, T. Enoki, M. Koshino and H. Tanaka, *Phys. Rev. B*, 2010, **81**, 115408.
66. E. Erdem, *J. Alloys Compd.*, 2014, **605**, 34-44.
67. P. Jakes and E. Erdem, *Phys. Status Solidi (RRL)*, 2011, **5**, 56-58.
68. R. Vidya, P. Ravindran, H. Fjellvåg, B. Svensson, E. Monakhov, M. Ganchenkova and R. M. Nieminen, *Phys. Rev. B*, 2011, **83**, 045206.
69. D. Liu, Y. Lv, M. Zhang, Y. Liu, Y. Zhu, R. Zong and Y. Zhu, *J. Mater. Chem. A*, 2014, **2**, 15377-15388.
70. A. J. Reddy, M. Kokila, H. Nagabhushana, J. Rao, C. Shivakumara, B. Nagabhushana and R. Chakradhar, *Spectrochimica Acta A*, 2011, **81**, 59-63.
71. A. Pöppl and G. Völkel, *Phys. Status Solidi (a)*, 1991, **125**, 571-581.
72. X. Xu, C. Xu, J. Dai, J. Pan and J. Hu, *J. Phys. Chem. Solids*, 2012, **73**, 858-862.
73. X. Chen, Y. Li, X. Pan, D. Cortie, X. Huang and Z. Yi, *Nat. Commun.*, 2016, **7**, 12273.
74. S. Moribe, T. Ikoma, K. Akiyama, Q. Zhang, F. Saito and S. Tero-Kubota, *Chem. Phys. Lett.*, 2007, **436**, 373-377.
75. Z. Hao, L. Fen, G. Lu, J. Liu, L. An and H. Wang, *Appl. Catal. A*, 2001, **213**, 173-177.
76. J. Cope and I. Campbell, *J. Chem. Soc., Faraday Trans.*, 1973, **69**, 1-9.
77. C. Gionco, M. C. Paganini, E. Giamello, R. Burgess, C. Di Valentin and G. Pacchioni, *Chem. Mater.*, 2013, **25**, 2243-2253.
78. F. Oba, A. Togo, I. Tanaka, J. Paier and G. Kresse, *Phys. Rev. B*, 2008, **77**, 245202.
79. S. Clark, J. Robertson, S. Lany and A. Zunger, *Phys. Rev. B*, 2010, **81**, 115311.
80. F. Gallino, G. Pacchioni and C. Di Valentin, *J. Chem. Phys.*, 2010, **133**, 144512.
81. A. R. Puigdollers, F. Illas and G. Pacchioni, *J. Phys. Chem. C*, 2016, **120**, 4392-4402.

82. S. Lany and A. Zunger, *Phys. Rev. B*, 2010, **81**, 113201.
83. N. Hsu, W. Hung and Y. Chen, *J.Appl. Phys.*, 2004, **96**, 4671-4673.
84. V. Subramanian, E. E. Wolf and P. V. Kamat, *J. Phys. Chem. B*, 2003, **107**, 7479-7485.
85. K. Vanheusden, C. Seager, W. t. Warren, D. Tallant and J. Voigt, *Appl. Phys. Lett.*, 1996, **68**, 403-405.
86. S. Vempati, J. Mitra and P. Dawson, *Nanoscale Res. Lett.*, 2012, **7**, 470.
87. T. K. Kundu, N. Karak, P. Barik and S. Saha, *Int. J. Soft Comput. Eng.*, 2011, **1**, 19-24.
88. W. Zhu, S. Kitamura, M. Boffelli, E. Marin, E. Della Gaspera, M. Sturaro, A. Martucci and G. Pezzotti, *Phys. Chem. Chem. Phys.*, 2016, **18**, 9586-9593.
89. N. Kondal and S. K. Tiwari, *Mater. Res. Bull.*, 2017, **88**, 156-165.
90. E. Epie and W. Chu, *Appl. Surf. Sci.*, 2016, **371**, 28-34.
91. F. Stavale, N. Nilius and H.-J. Freund, *J. Phys. Chem. Lett.*, 2013, **4**, 3972-3976.
92. C. Chandrinou, N. Boukos, C. Stogios and A. Travlos, *Microelectron. J.*, 2009, **40**, 296-298.
93. W.-C. Sun, Y.-C. Yeh, C.-T. Ko, J.-H. He and M.-J. Chen, *Nanoscale Res. Lett.*, 2011, **6**, 556.
94. C. Drouilly, J. M. Krafft, F. Averseng, S. Casale, D. Bazer-Bachi, C. Chizallet, V. Lecocq, H. Vezin, H. Lauron-Pernot and G. Costentin, *J. Phys. Chem. C*, 2012, **116**, 21297-21307.
95. P. Rauwel, M. Salumaa, A. Aasna, A. Galeckas and E. Rauwel, *J. Nanomater;*, 2016, **2016**, 19.
96. M. Liu, A. Kitai and P. Mascher, *J. Lumin.*, 1992, **54**, 35-42.
97. X. Wu, G. Siu, C. Fu and H. Ong, *Appl. Phys. Lett.*, 2001, **78**, 2285-2287.
98. S. Limpijumnong, X. Li, S.-H. Wei and S. Zhang, *Appl. Phys. Lett.*, 2005, **86**, 211910.
99. S. Sugiura, Y. Shibuta, K. Shimamura, M. Misawa, F. Shimojo and Y. Shu, *Solid State Ionics*, 2016, **285**, 209-214.

Electronic Supplementary Information for

Defect-related multicolour emissions in ZnO tetrapods: from violet, over green to yellow

Miao Zhang[1,2] Frédéric Averseng[1], Francia Haque[2], Patrizia Borghetti[2], Jean-Marc Krafft[1], Benoît Baptiste[3], Guylène Costentin[1*] and Slavica Stankic[2*]

[1]Sorbonne Université, CNRS, Laboratoire de Réactivité de Surface, LRS, F-75005 Paris, France

[2]Sorbonne Université, CNRS, Institut des NanoSciences de Paris, INSP, F-75005 Paris, France.

[3]Sorbonne Université, CNRS, Institut de Minéralogie, de Physique des Matériaux et de Cosmochimie, IMPMC, F-75005 Paris, France

[*]Corresponding authors: guylene.costentin@upmc.fr and slavica.stankic@insp.jussieu.fr

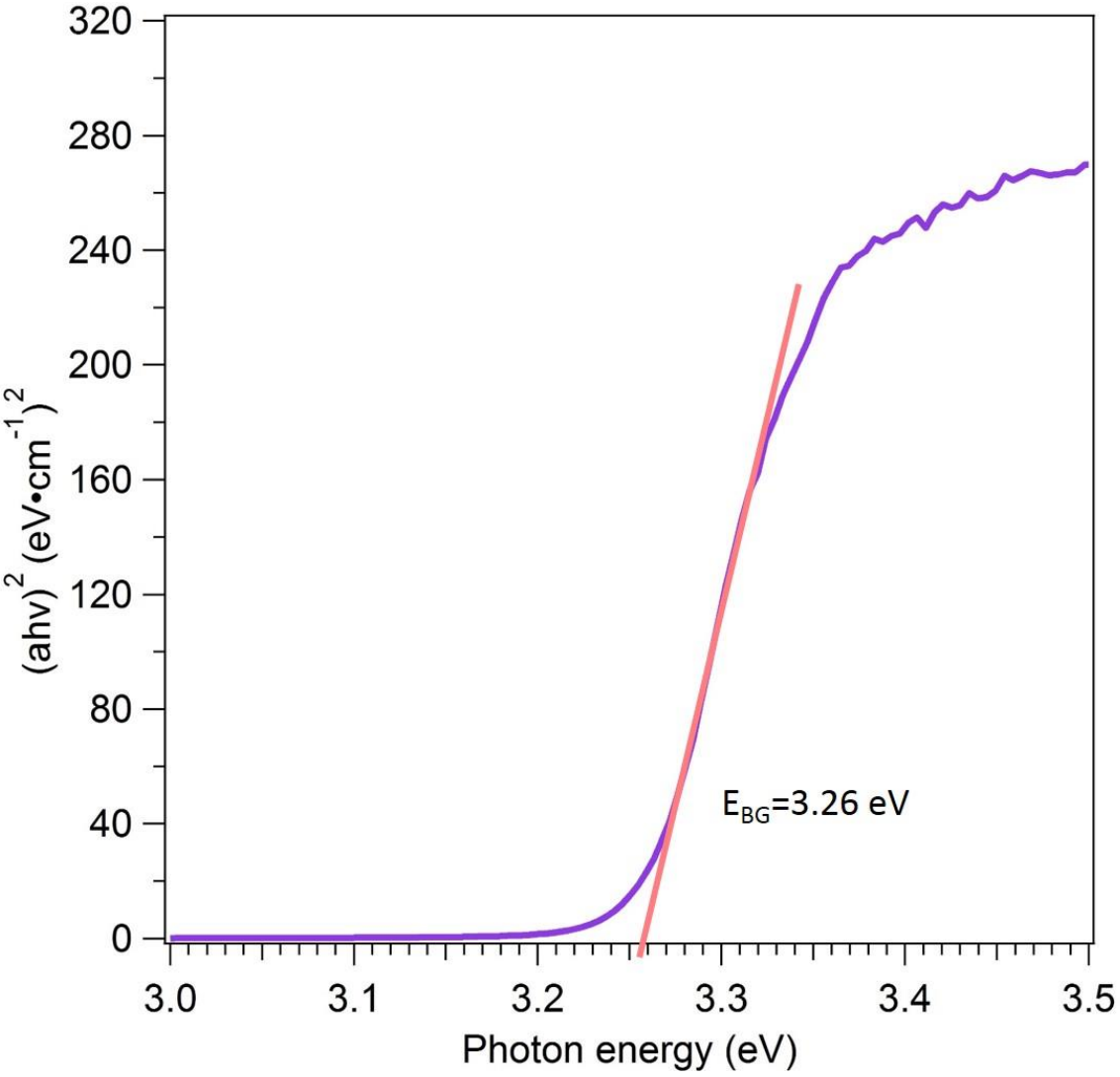

Figure SI-1. Tauc plot of as-synthesized ZnO smoke.

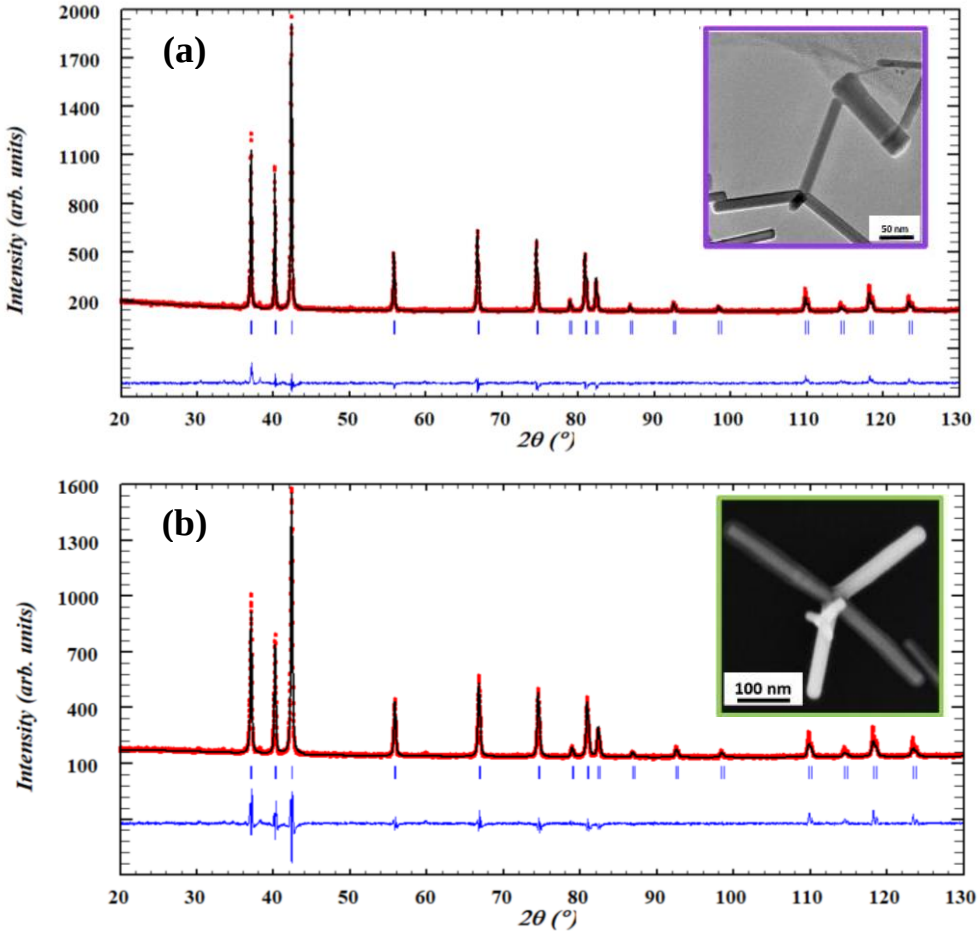

Figure SI-2. XRD and Rietveld refinements of the (a) as-synthesized and (b) annealed (773 K and P < 10^{-5} mbar) ZnO smoke. For both, the red crosses are the experimental points, the black line is the calculated pattern, blue vertical tick marks refer to Bragg reflections, and the blue line is the calculated difference pattern. The insets represent TEM and SEM images for as-synthesized and annealed sample, respectively.

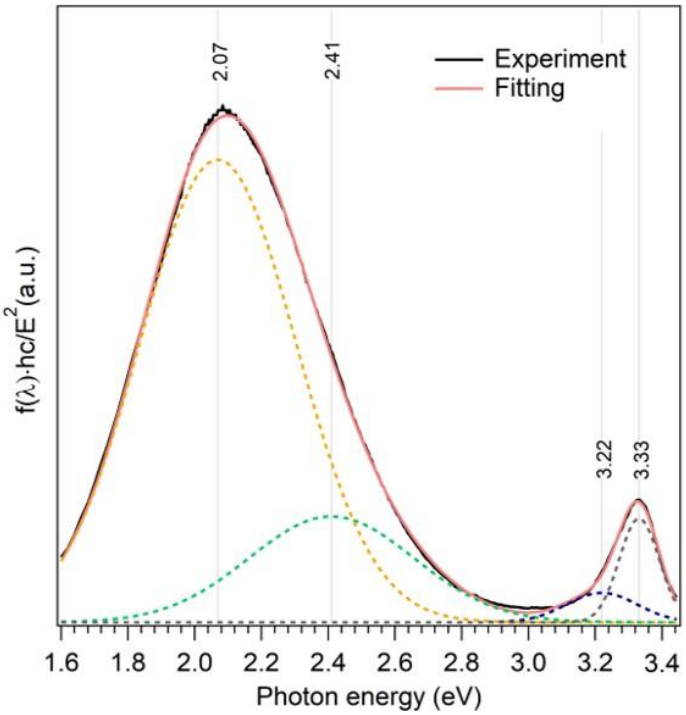

Figure SI-3. PL spectrum and corresponding band fitting analysis of ZnO sample three times annealed (T = 773 K) in P_{O2} = 100 mbar.